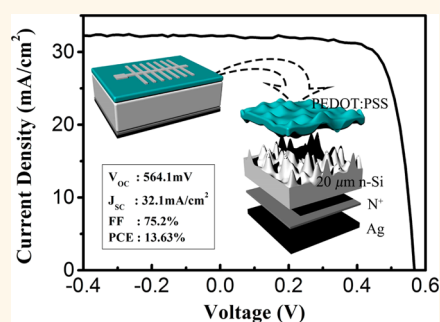


Realization of 13.6% Efficiency on 20 μm Thick Si/Organic Hybrid Heterojunction Solar Cells *via* Advanced Nanotexturing and Surface Recombination Suppression

Jian He,[†] Pingqi Gao,^{*,†} Mingdun Liao,[†] Xi Yang,[†] Zhiqin Ying,[†] Suqiong Zhou,[†] Jichun Ye,^{*,†} and Yi Cui^{*,‡}

[†]Ningbo Institute of Material Technology and Engineering, Chinese Academy of Sciences, Ningbo 315201, People's Republic of China and [‡]Department of Material Science and Engineering, Stanford University, Stanford, California 94305, United States

ABSTRACT Hybrid silicon/polymer solar cells promise to be an economically feasible alternative energy solution for various applications if ultrathin flexible crystalline silicon (c-Si) substrates are used. However, utilization of ultrathin c-Si encounters problems in light harvesting and electronic losses at surfaces, which severely degrade the performance of solar cells. Here, we developed a metal-assisted chemical etching method to deliver front-side surface texturing of hierarchically bowl-like nanopores on 20 μm c-Si, enabling an omnidirectional light harvesting over the entire solar spectrum as well as an enlarged contact area with the polymer. In addition, a back surface field was introduced on the back side of the thin c-Si to minimize the series resistance losses as well as to suppress the surface recombination by the built high–low junction. Through these improvements, a power conversion efficiency (PCE) up to 13.6% was achieved under an air mass 1.5 G irradiation for silicon/organic hybrid solar cells with the c-Si thickness of only about 20 μm . This PCE is as high as the record currently reported in hybrid solar cells constructed from bulk c-Si, suggesting a design rule for efficient silicon/organic solar cells with thinner absorbers.



KEYWORDS: hybrid solar cell · heterojunction · surface nanotexturing · charge recombination · light trapping

Hybrid heterojunction solar cells (HHSCs) currently receive growing attention in the field of renewable energy due to the low fabrication costs and considerable efficiencies.^{1–3} In particular, hybrid cells made of p-type-conjugated polymer film, poly(3,4-ethylene dioxithiophene):poly(styrenesulfonate) (PEDOT:PSS), and n-type crystalline silicon (c-Si) substrate show great potential in the fast improvement of power conversion efficiency (PCE). For these kinds of HHSCs, generally, the n-type c-Si acts as the light-absorbing layer, where electron–hole pairs are generated. The PEDOT:PSS acts as the hole transport layer, while electron–hole pairs are separated at Si/PEDOT:PSS interfaces due to the Schottky barrier of the heterojunction. By a simple spin-coating process at room temperature followed with a short-time annealing at low temperature, conjugated PEDOT:PSS is

uniformly coated on c-Si substrate and thus the functional heterojunction is formed. Meanwhile, the front c-Si surface can be perfectly passivated by the PEDOT:PSS if a full coverage is achieved. Therefore, the interface recombination losses are negligibly small, and thus the open-circuit voltage (V_{oc}) could be approaching the upper limit. Furthermore, the hole mobility and conductance in PEDOT:PSS are much higher than those of most other polymers, which reduces the series resistance and enables a sufficiently high short-circuit current density (J_{sc}).^{4,5}

Despite the significant progress recently, this type of c-Si/PEDOT:PSS hybrid solar cell cannot be practically used unless the cost is reduced. An effective approach for the cost reduction is to use thin c-Si films as active absorbers to replace bulk Si (over 300 μm in most of the reported work). Thinner c-Si films also allow for possible use of a lower

* Address correspondence to gaopingqi@nimte.ac.cn, jichun.ye@nimte.ac.cn, yicui@stanford.edu.

Received for review April 24, 2015 and accepted June 5, 2015.

Published online 10.1021/acs.nano.5b02432

© XXXX American Chemical Society

quality Si with shorter carrier diffusion lengths, representing another aspect of cost reduction.⁶ Additionally, thinner c-Si films minimize the Auger recombination, leading to a larger V_{OC} and fill factor (FF).⁷ Furthermore, thin c-Si introduces new features, such as light weight and flexibility, expanding the applications of hybrid solar cells to many special circumstances. However, despite the above-mentioned potential advantages, two main problems (*i.e.*, insufficient light absorption and severe surface recombination) occur when an ultrathin c-Si substrate is used. The surface texturing for c-Si thin film plays a decisive role for effective light trapping and thus the final device efficiency.^{8,9} Regarding the surface recombination, it becomes a relatively more significant limiting factor to the J_{SC} and V_{OC} because the bulk recombination is reduced for the thin c-Si.¹⁰

For the conventional bulk c-Si/PEDOT:PSS HHSCs, PCEs over 13% have been reported through the improvements in the interface properties, either on the front or the rear side of the c-Si.^{11–14} For example, a 13.3% PCE was achieved with a V_{OC} of 564 mV and a J_{SC} of 32.6 mA cm⁻² by modifying the PEDOT:PSS and reducing the defect density at Si/PEDOT:PSS interfaces.¹³ Sun *et al.* developed a series of methods for the modification on c-Si surfaces, including the front surface passivation using methyl groups, the back surface contact improvement by inserting an ultrathin organic layer with a wide band gap,¹⁵ and the anti-reflection improvement by a MoO₃ layer on the front surface, to achieve a record PCE of 13.8% with a sufficiently high V_{OC} of 630 mV.¹² However, the J_{SC} is relatively low (29.2 mA cm⁻²) in this record cell, due to the poor light harvesting of the planar c-Si substrate without any surface texturing. The attempts of using surface texturing, including the traditional random pyramids,¹⁶ the nanostructures,^{11,17} and the hierarchical structures,^{18,19} were successfully realized on c-Si/polymer hybrid solar cells to effectively boost the light absorption. Unfortunately, the quality of polymer/silicon junctions was deteriorated due to the incomplete coverage of the polymer layer, resulting in a severe carrier recombination and thus a low V_{OC} .¹¹ Jung *et al.* achieved a 10.03% efficiency on Si nanorod/PEDOT:PSS HHSCs with a V_{OC} of 510 mV, even with a back surface field (BSF) of a highly doped N⁺-Si layer.²⁰ Recently, an interface engineering method, that is, inserting a conformal layer of small molecules between Si and PEDOT:PSS, partially resolved the issue of the incomplete surface coverage and the severe interface recombination in hybrid cells with nanotexturing. As a result, a PCE of 13.01% was achieved, while the V_{OC} was still under 550 mV, which restricted further improvements on efficiency.¹¹ So it is really crucial to develop novel surface nanostructures with low aspect ratio and excellent antireflection performance for the junction area increase and the light-trapping boost

simultaneously, which ensures both large J_{SC} and V_{OC} for ultrathin c-Si/PEDOT:PSS HHSCs.

Here, we developed a facile method to produce hierarchically structured Si nanopores (SiNPs) on 20 μ m thick c-Si films, which were further used as substrates for the construction of Si/PEDOT:PSS HHSCs. The hierarchically structured SiNPs fabricated by a novel metal-assisted chemical etching (MaCE) process had second-ordered nanostructures on the side walls of bowl-like nanopores. As predicted, this novel hierarchical nanostructure, serving as surface texturing, significantly improved light absorption in thin c-Si. Meanwhile, the primary bowl-like nanopores and the second-ordered tiny nanostructures effectively enlarged the contact area between c-Si and PEDOT:PSS, which partially mitigated the extent of V_{OC} deterioration caused by the incomplete coverage. A highly doped N⁺-BSF layer was introduced on the back side of the c-Si thin film to further reduce the contact resistance and suppress the electronic recombination by the established high–low junction. With the advantages mentioned above in front-side antireflection, junction coverage, carrier collection efficiency, and back-side contact properties, our best cell shows a 64.6% enhancement in PCE, from 8.26 to 13.63%, when compared with the flat counterpart without the BSF structure.

RESULTS AND DISCUSSION

Figure 1 illustrates the structural schematics and the corresponding energy band diagrams of c-Si/PEDOT:PSS HHSCs with different configurations of front surface texturing and/or BSF. For the conventionally nanopore-structured (conventional-SiNPs) cells, as shown in the top image of Figure 1a, the relatively high aspect ratio of SiNPs and long carbon chains of PEDOT:PSS make the conducting polymer film hover above the SiNPs. Thus, ultrahigh surface area, prolonging the bare side walls of the SiNPs, introduces a high density of recombination centers. Photogenerated electrons have a great chance of being trapped by the high-density surface defects before being collected by the external circuit, as shown in the energy band diagram in Figure 1a, resulting in an unexpected potential drop and thus the performance deterioration, including low J_{SC} , V_{OC} , FF. In order to reduce the surface recombination, bowl-like nanopores in larger feature sizes that are formed from the conventional-SiNPs *via* a chemical reconstruction process (reconstructed-SiNPs) are favorable to enable a complete coverage of PEDOT:PSS, as shown in Figure 1b. With the full coverage, most of the SiNPs are well-passivated and the density of the interfacial recombination centers could be sufficiently reduced (the energy band diagram is shown in Figure 1b). Similarly, the back surface of c-Si also has a high density of surface traps, resulting in a high surface recombination, a large reverse saturation current, and a deteriorated ideal

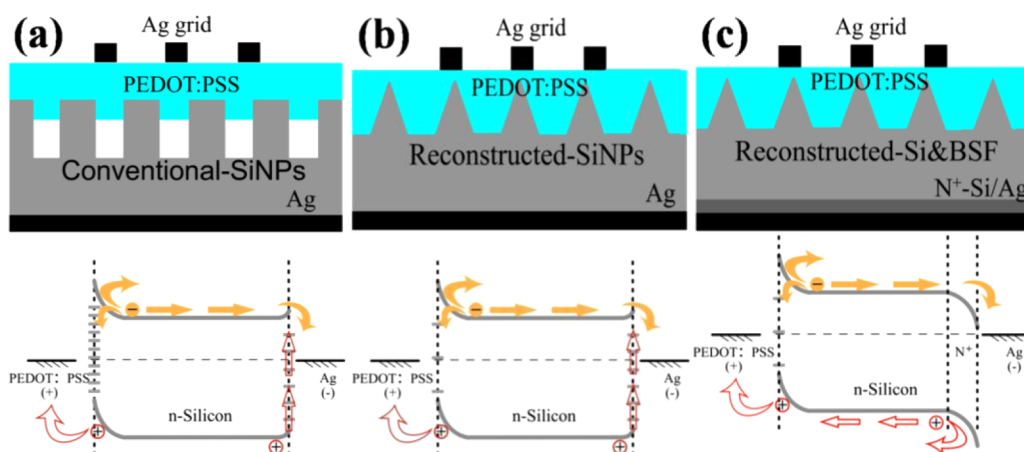


Figure 1. Schematics of the device structures and the energy band diagrams of thin film c-Si/PEDOT:PSS hybrid solar cells with surface texturing of (a) conventional-SiNPs, (b) reconstructed-SiNPs, and (c) reconstructed-SiNPs combined with the highly doped BSF layer (N^+ -Si). The gray spots in n-Si energy gap represent the recombination centers. For the conventional-SiNP structure, large recombination centers are present at the interface of Si/PEDOT:PSS. The arrows represent the migration of carriers.

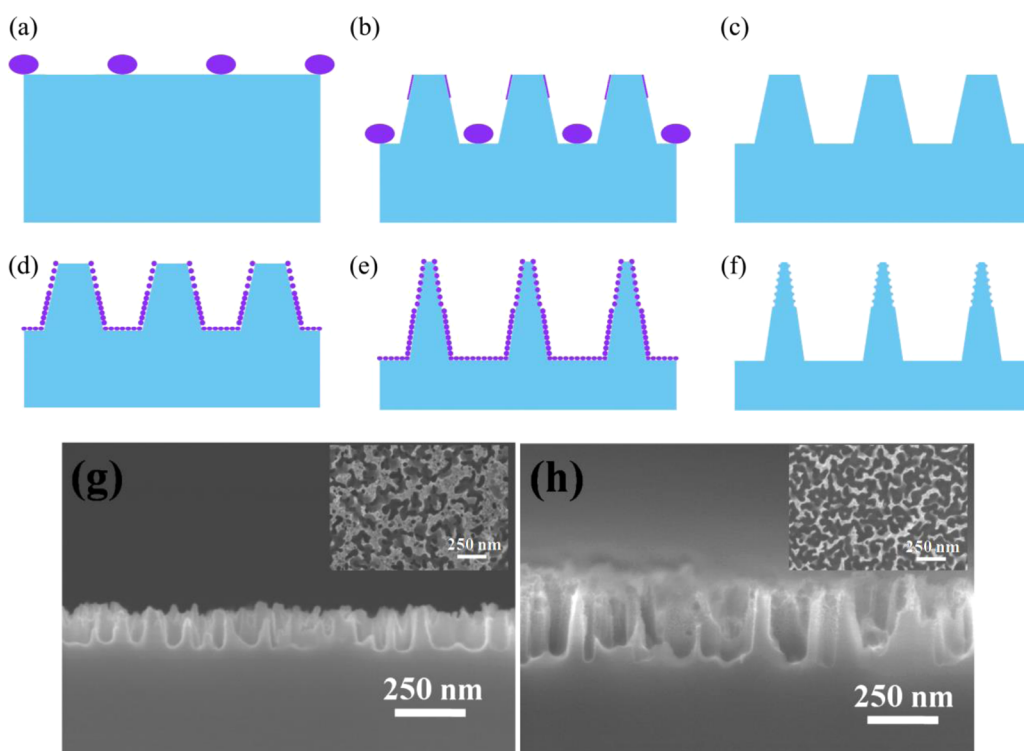


Figure 2. (a–f) Schematics of the fabrication flow for the hierarchically structured SiNPs using a novel MaCE process. (a) Ag nanoparticle deposition in the first round of the MaCE process. (b) Ag-assisted chemical etching to form SiNPs, accompanied by Ag deposition on the side wall while etching. (c,f) Removal of Ag nanoparticles in concentrated HNO_3 . (d) Ag nanoparticle deposition in the second round of the MaCE process. (e) Reconstruction of SiNPs assisted by Ag nanoparticles. (g) Cross-sectional SEM images of SiNPs after the first round of the MaCE process and (h) after the second round of the MaCE process. The insets in (g,h) show the top view of SiNPs after the first and second rounds of the MaCE process, respectively.

factor of the Si/PEDOT:PSS junction. Additionally, the direct contact of a metal layer (*e.g.*, Ag) with the moderately doped c-Si, as shown in Figure 1a,b, generally forms a Schottky barrier at the metal–semiconductor interface (at the back side of the ultrathin c-Si), leading to an increase in contact resistance and thus a decrease in both FF and V_{OC} . These two issues can be resolved through an introduction of a highly doped N^+ layer between the n-Si and the back-side metal electrode,

as shown in Figure 1c. This N^+ layer not only directly improves the contact properties but also delivers a back surface field that effectively reduces the recombination rate at the back surface *via* a downward band bending for reflecting holes (minority carrier).^{10,21,22}

Experimentally, the reconstructed-SiNPs with enlarged pore diameter were achieved using a novel MaCE process, which is illustrated in Figure 2a–f. For the conventional MaCE process, the Ag ions were

first deposited on the Si surface *via* an electrodeless process in the AgNO_3 and HF solution, and the isotropic etching process was initiated once the sample was transferred into the etchant solution of HF and H_2O_2 .^{23,24} On the contrary, in our study, a MaCE process with a solution comprising AgNO_3 , H_2O_2 , and HF was used to avoid the solely vertical etching of SiNPs. In this etching process, the deposition of Ag ions and the formation of SiNPs took place simultaneously, as illustrated in Figure 2a–c. Especially in the etchant with concentrated AgNO_3 , the deposited Ag almost formed a continuous film while etching, which efficiently suppresses the depth increase of SiNPs.²⁵ After the removal of the residual Ag particles in concentrated HNO_3 , the samples were returned to the original solution (AgNO_3 , H_2O_2 , and HF) for a continued MaCE process. In the second round of the MaCE process, the Ag nanoparticles were deposited again on the surfaces of SiNPs rather than the originally flat Si surface (Figure 2d), resulting in a more isotropic Si removal and an enlarged pore of SiNPs. During the etching process, the deposition and dissolution of Ag reached a dynamical balance,²⁶ and the porous Si layer on the side wall and apex of SiNPs caused by the first round of the MaCE process enlarged the contact areas with the etchant, which intensified the Ag/Ag⁺ redox pair circulation. As a result, the density of Ag nanoparticles on the apex was relatively low, and it gradually became higher when approaching the bottoms of SiNPs, leading to a structure with smooth bottoms and rough apices, as illustrated in Figure 2e,f. Figure 2g,h shows the scanning electron microscope (SEM) images of the fabricated SiNPs after the first and second rounds of the MaCE process, respectively. The top views of SiNPs are also present in the inset images in Figure 2g,h. It is clear to see that the first round of etching produced shallow SiNPs with “V-shape” structures, while the second round of the MaCE process reconstructed the SiNPs into enlarged nanopores with rough apices that were filled with second-ordered nanostructures, confirming the proposed mechanisms shown in Figure 2a–f. Additionally, combined with the enlarged diameter of SiNPs, the density of SiNPs was efficiently decreased after the second round of the MaCE reconstruction by partially polishing the SiNPs, which is also clearly shown in the inset images in Figure 2g,h. Compared with the SiNPs fabricated by the conventional MaCE process (as shown in Supporting Information Figure S2), our reconstructed-SiNPs exhibit a larger feature size and a shallower depth, showing inherent advantages for hybrid solar cell fabrication.

In order to achieve a large J_{SC} , efficient light harvesting in all usable solar spectra for thin c-Si films is required. Figure 3a compared the reflectance of 20 μm thick c-Si films in flat (in black) and structured by the conventional-SiNPs (in red) by the reconstructed-SiNPs (in blue). For comparison, the reflection spectrum of the

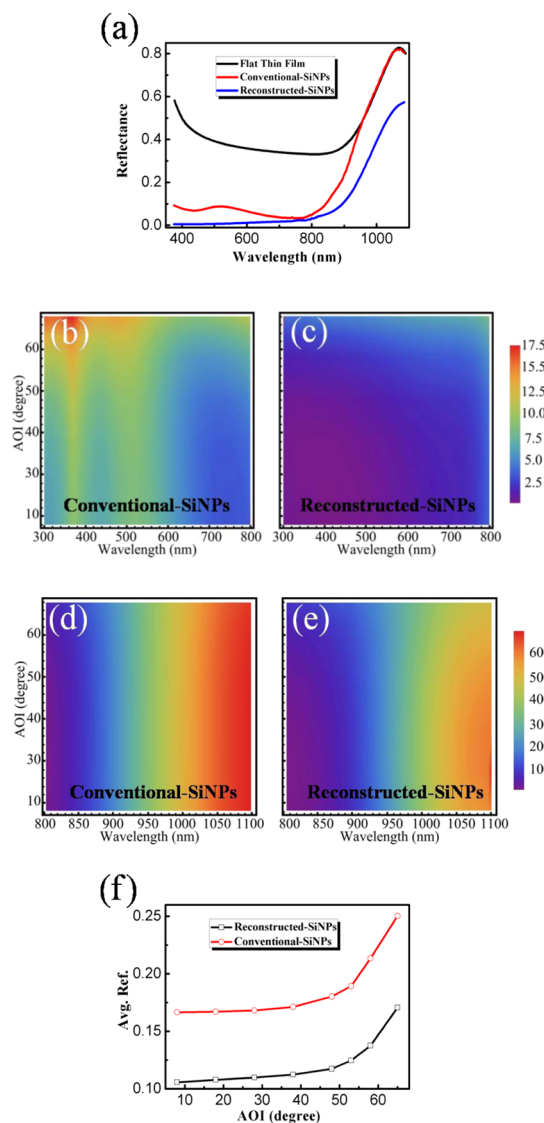


Figure 3. (a) Reflection spectra of 20 μm thick thin film c-Si with flat, conventional-SiNP, and reconstructed-SiNP surface texturing in the whole wavelength range. (b–e) AOI-dependent reflectance spectra of conventional-SiNPs and reconstructed-SiNPs at a wavelength range of 300–800 and 800–1100 nm, respectively. (f) Averaged reflectance in full wavelength range of conventional-SiNPs and reconstructed-SiNPs at different AOIs.

interim SiNPs just after one round of the etching process is also shown in Supporting Information Figure S3. With a high aspect ratio of nanostructures, the conventional-SiNPs had a reasonably good antireflection performance in the visible light wavelength region (400–800 nm), while the reflection beyond 800 nm wavelength was rapidly increased and reached as high as that of the flat thin film. For the reconstructed-SiNPs, a significant reduction of reflectance over the entire wavelength range was achieved. This light-harvesting improvement observed in the near-ultraviolet wavelength region for the reconstructed-SiNPs could be attributed to the second-ordered nanostructures on the apex, and the enhancement in the near-infrared/infrared wavelength

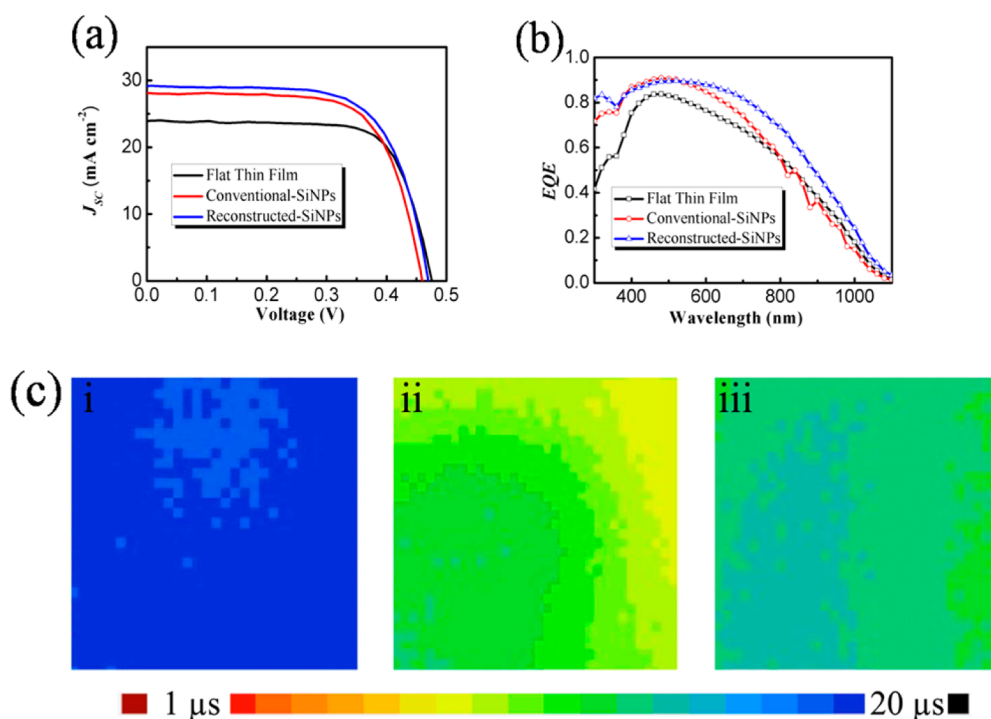


Figure 4. (a) Current density–voltage (J – V) curves, (b) EQE characteristics, and (c) minority carrier lifetime mapping of thin film Si/PEDOT:PSS HHSCs with different surface texturing, (i) without surface texturing; (ii) conventional-SiNPs; (iii) reconstructed-SiNPs.

TABLE 1. Photovoltaic Characteristics of the Flat, Conventional-SiNP-Structured, and Reconstructed-SiNP-Structured 20 μ m Thick Si/PEDOT:PSS HHSCs with and without the Highly Doped BSF Layer

| samples ^a | | V_{oc}^b (mV) | J_{sc}^b (mA cm ⁻²) | FF ^b (%) | PCE ^b (%) | R_s^b ($\Omega \cdot \text{cm}^{-2}$) | J_0^b (A cm ⁻²) | n^b |
|----------------------|--------------------|--------------------|-----------------------------------|---------------------|----------------------|---|-------------------------------|-------------|
| thin flat films | without BSF | 475.7 | 23.9 | 72.7 | 8.26 | 9.5 | 5.0×10^{-7} | 1.86 |
| | | 472.5(± 1.5) | 23.7(± 0.3) | 71.5(± 0.8) | 8.05(± 0.3) | 9.3(± 0.8) | | |
| | with BSF | 585.5 | 26.8 | 75.7 | 11.90 | 6.7 | 1.8×10^{-8} | 1.61 |
| | 583.6(± 1.2) | 26.6(± 0.3) | 74.5(± 0.8) | 11.56(± 0.3) | 6.3(± 0.6) | | | |
| conventional-SiNPs | without BSF | 459.6 | 28.1 | 65.6 | 8.47 | 9.3 | 6.8×10^{-6} | 2.38 |
| | | 460.5(± 2.1) | 27.8(± 0.4) | 64.2(± 0.6) | 8.22(± 0.3) | 9.4(± 0.6) | | |
| | with BSF | 557.1 | 31.0 | 70.0 | 12.10 | 7.6 | 7.0×10^{-7} | 2.03 |
| | 554.1(± 1.8) | 30.6(± 0.8) | 68.4(± 1.4) | 11.60(± 0.6) | 7.0(± 0.6) | | | |
| reconstructed-SiNPs | without BSF | 469.2 | 29.1 | 67.8 | 9.27 | 9.6 | 1.5×10^{-6} | 2.13 |
| | | 470.3(± 1.5) | 28.9(± 0.3) | 66.7(± 0.8) | 9.06(± 0.2) | 9.5(± 0.5) | | |
| | with BSF | 564.1 | 32.1 | 75.2 | 13.63 | 6.5 | 1.4×10^{-7} | 1.86 |
| | 561.8(± 2.0) | 32.0(± 0.5) | 73.8(± 1.2) | 13.26(± 0.4) | 6.3(± 0.7) | | | |

^aData and statistics based on 10 cells of each condition. ^bNumbers in bold are the maximum values.

region may be related to the bowl-like structure of the reconstructed-SiNPs, resulting in a graded effective refractive index and thus an excellent impedance matching effect.²⁷

In addition to the reflectance measurement on normal incidence, angle of incidence (AOI)-dependent reflectance (R_{AOI}) was measured to investigate the omnidirectional light-harvesting ability of the conventional-SiNPs and reconstructed-SiNPs, as shown in Figure 3b–e. For the conventional-SiNPs in Figure 3b,d, the reflectance cannot be efficiently suppressed at the wavelength range below 600 nm and above 950 nm at all of the AOIs, which results from the high reflective index of c-Si at short wavelength range and the high aspect ratio of

SiNPs. However, for the reconstructed-SiNPs, as shown in Figure 3c,e, the R_{AOI} is efficiently suppressed at all AOIs and in the entire wavelength range due to the hierarchical structure and the excellent impedance matching effect of the bowl-like structure. Figure 3f shows the average reflectance in the whole wavelength range of 300–1100 nm at different AOIs, showing an angle independence property of the reconstructed-SiNPs.

The current density–voltage (J – V) curves of the three types of 20 μ m thick c-Si/PEDOT:PSS HHSCs made from the flat film, the conventional-SiNPs, and the reconstructed-SiNPs are illustrated in Figure 4a, and their main characteristic parameters are listed in Table 1. The best cell with the reconstructed-SiNPs shows a

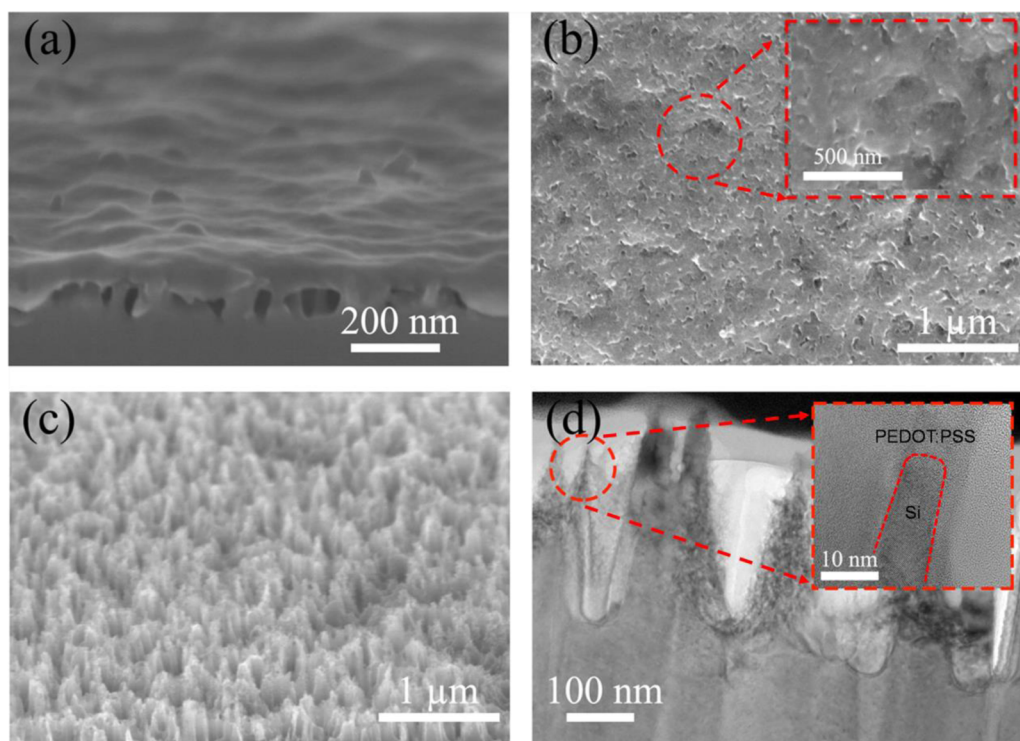


Figure 5. (a) Cross-sectional SEM image of reconstructed-SiNPs covered with PEDOT:PSS with a 10° tilt. (b) SEM image of the mechanically peeled PEDOT:PSS film from the reconstructed-SiNP-structured cell. The inset shows a detailed view of the designated area. (c) Cross-sectional SEM image with a 20° tilt of the reconstructed-SiNPs after peeling the PEDOT:PSS film. (d) TEM image of reconstructed-SiNPs coated with PEDOT:PSS. The inset image shows a detailed view of the Si/PEDOT:PSS interface from the designated area.

V_{OC} of 469.2 mV, J_{SC} of 29.1 mA cm⁻², FF of 67.8%, and PCE of 9.27%, representing nearly a 22.0% enhancement in J_{SC} and 12.2% in PCE in comparison to the flat counterpart. The J_{SC} of the cell with the conventional-SiNPs is lower than the restructured one, indicating that the hierarchical SiNPs have better light-harvesting properties that are consistent with the reflectance measurement. A careful examination on the external quantum efficiency (EQE) curves (Figure 4b) and the reflection spectra (Figure 3a) shows that the enhancement of J_{SC} for the cell with reconstructed-SiNPs is mainly caused by the increased absorption in the near-infrared wavelength region of 900–1100 nm and the short wavelength region below 400 nm. Meanwhile, the average V_{OC} values for the flat cells, the cells with the conventional-SiNPs, and the cells with the reconstructed-SiNPs were 475.7, 459.5, and 469.2 mV, respectively, implying different passivation properties by the PEDOT:PSS layers. Both of the SiNP structures had a V_{OC} lower than that of the flat counterpart. The V_{OC} for the reconstructed-SiNP sample is higher than that of the conventional-SiNPs, which confirms that our initial designs on coverage improvement do play an important role on the V_{OC} .

Figure 4c illustrates the minority carrier lifetime mapping measurements based on a microwave photoconductance decay technique for different surface-structured samples coated with PEDOT:PSS. In a

c-Si-based solar cell, the effective minority carrier lifetime is determined by both the bulk recombination and the surface recombination.⁷ For these three samples with similar thickness, the variations of measured minority carrier lifetime represent the surface recombination properties at the Si/PEDOT:PSS interface, assuming the identical bulk recombination. The average minority carrier lifetimes for the conventional-SiNP and the reconstructed-SiNP samples were 10.5 and 12.4 μ s, respectively, both lower than the flat one, 18.4 μ s. The degradations of structured samples over the flat one were mainly induced by the uncovered areas in the bottom parts of the SiNPs, where severe carrier recombination occurred. The microwave photoconductance decay measurements further confirmed that the cell with reconstructed-SiNPs has less V_{OC} drop compared with the conventionally structured one, and there is further room for optimization to meet or even exceed the flat one.

The improvement in the electrical properties of the reconstructed cells is also associated with the modified interface between the organic and the c-Si. Figure 5a shows the cross-sectional SEM image of the reconstructed-SiNPs covered with the PEDOT:PSS layer. The mechanically peeled PEDOT:PSS film and the underneath reconstructed-SiNPs are also present in Figure 5b,c. Compared to the conventional-SiNPs (as shown in Supporting Information Figure S2b), the

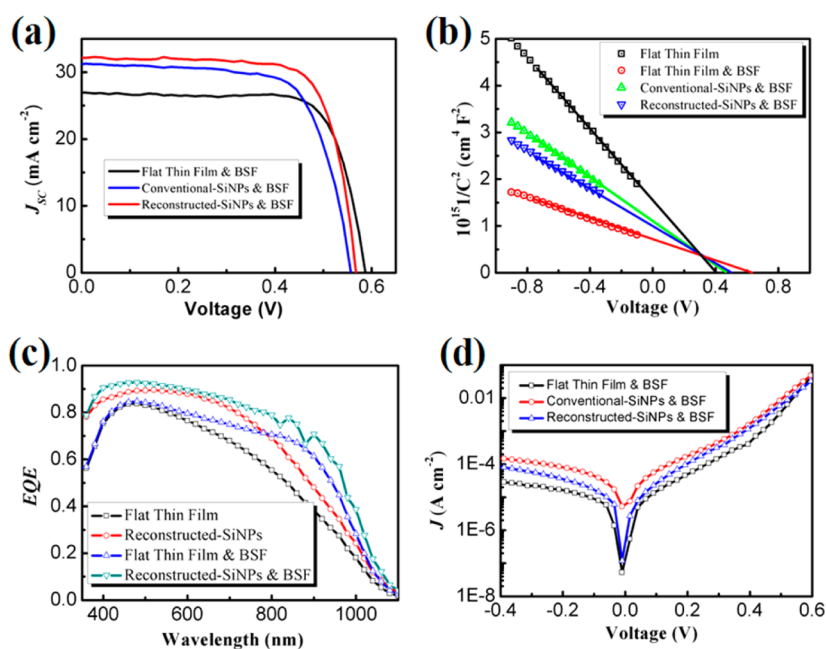


Figure 6. (a) J - V curves of the BSF-combined 20 μm thick c-Si/PEDOT:PSS HHSCs with and without surface texturing. (b) C^{-2} - V plots of the flat thin film hybrid solar cells with and without the BSF layer, as well as the BSF-combined cells with different surface texturing. (c) EQE characteristics of the flat and reconstructed thin film Si/PEDOT:PSS HHSCs with and without the BSF layer. (d) Dark J - V characteristics of the BSF-combined thin film Si/PEDOT:PSS HHSCs with different surface texturing.

reconstructed-SiNP cell shows a more conformal contact between c-Si and the PEDOT:PSS film, due to the larger size and lower density of the SiNPs. A wavy surface topography was observed in Figure 5b, which was caused by the conformal contact. The dense indentation on the PEDOT:PSS film was caused by the tips of the SiNPs, as well as the second-ordered tiny nanostructures. This will provide increased contact area for the p-n junction and further improve the efficiency of carrier separation and collection. After the PEDOT:PSS film was peeled, no polymer residues were left on the Si substrate, as shown in Figure 5c. Figure 5d shows a high-resolution transmission electron microscope (HR-TEM) image that was collected from the apex for the reconstructed-SiNP structures coated with PEDOT:PSS. Additional HR-TEM images of the reconstructed-SiNP/PEDOT:PSS interface are shown in Supporting Information Figure S4. The interfaces of PEDOT:PSS and Si are indicated by red dashed lines for clarity. A selected area diffraction (SAD) pattern is also shown in Figure S4c, which confirms the single-crystalline structure of the Si nanostructures. The HR-TEM images in Figure S4a,b clearly show that our two-round MaCE process has the capability of providing atomically smooth Si surfaces, which is quite different from the results of previously reported SiNPs fabricated by conventional MaCE, where rough side wall surfaces were always created.²⁶ The atomically smooth surfaces together with the conformal coating of polymer film are beneficial to reduce the surface recombination. According to the structure images and

electronic parameters demonstrated above, it can be concluded that the novel hierarchical nanostructure has the inherent structural advantages for polymer coverage.

In order to further improve the back-side contact performance and to decrease the electron-hole recombination at the back surface of the HHSCs, a highly doped N^+ -BSF layer was introduced. Figure 6a shows the J - V characteristics of the BSF-integrated thin film HHSCs with different surface texturing. The related photovoltaic parameters are summarized in Table 1. The series resistances (R_s) were effectively reduced for all of the cells with the BSF layer, indicating that the back-side contact was much improved. After the BSF layer was employed, the reconstructed-SiNP cell shows an improved performance with a V_{OC} of 564.1 mV, J_{SC} of 32.1 mA cm^{-2} , FF of 75.2%, and PCE of 13.63%. Capacitance-Voltage (C - V) measurements were used to examine the electronic performance of the devices with and without the BSF layer.^{14,28} As shown in Figure 6b, the insertion of the BSF layer in the flat sample results in a positive shift of the built-in voltage (V_{bi}) by about 20 mV. This leads to a formation of a favorable internal electrical field for the movement of electrons toward the cathode and for the confinement of holes on the Si side. When the BSF is applied in the cells with the conventional-SiNPs and the reconstructed-SiNPs, the values of V_{bi} are affected by the front interface, and the cell with reconstructed-SiNPs has a larger V_{bi} compared to the one with conventional-SiNPs.

Figure 6c shows the EQE characteristics of the flat and the reconstructed thin film Si/PEDOT:PSS HHSCs with and without the BSF layer. For the cell with reconstructed-SiNPs and BSF, a calculated J_{SC} of 31.7 mA cm^{-2} was confirmed by integrating the EQE with a standard AM1.5 solar spectrum. This value is consistent with the J_{SC} measured by the $J-V$ test (32.1 mA cm^{-2}), confirming the accurate definition of the device area when testing implementation. The testing procedure is elaborately addressed in Supporting Information in combination with the images of the real devices (Figure S6). As discussed previously, the insertion of the BSF layer mostly reduces the recombination at the back surface, showing the improvement of EQE in the long wavelength range of 600–1100 nm. For the reconstructed-SiNP cell, the insertion of BSF causes an unexpected improvement in the short wavelength range of 400–600 nm, approaching an EQE value higher than 90%. A possible hypothesis for this improvement is that, for thin film cells, the carrier diffusion length is much larger than the thickness of c-Si, and thus the strong built-in electric field and the improved electric contact at the back surface may eventually facilitate the separation and diffusion of the minority carrier at the front heterojunction and possibly suppress carrier recombination on those uncovered areas of SiNPs. However, for the flat thin film HHSC, the improvement of the BSF layer on the front heterojunction is negligible because of the well-passivated organic–inorganic interface.

To further evaluate the device performance of the differently structured HHSCs, the steady-state $J-V$ characteristics of the devices with the BSF layer in the dark are compared in Figure 6d (the devices without the BSF layer are shown in Supporting Information Figure S5 for comparison). The $J-V$ curves of all the devices exhibit rectifying characteristics, and a significant suppression of the reverse saturation current (J_0),

over 1 order of magnitude, is achieved for the devices with the BSF layer, as can be seen from Table 1. After structured with nanopores on the front surface, the reverse saturation current and ideal factor are deteriorated by the front interface recombination. For the c-Si substrate with the reconstructed-SiNPs, the top surface was much better covered by the PEDOT:PSS film compared to the one with conventional-SiNPs, and a lower extent of carrier recombination occurred, as can be validated by the values of the J_0 and ideal factor (n) in Table 1. This suggests that the band bending caused by BSF at the rear and the Schottky barrier at the front heterojunction both play an important role in the improvement in the collection efficiency of the photo-generated carriers.

CONCLUSION

In conclusion, we developed hierarchically structured SiNPs with a large feature size for the application of hybrid heterojunction solar cells by a novel metal-assisted chemical etching process. This hierarchical SiNP not only delivered excellent light trapping but also formed an improved contact at the SiNP/polymer interface. The deliberate geometry design on surface nanotexturing offers a possible way out of the impasse of balancing in electrical and optical characteristics related to conventional nanostructures. Combined with the highly doped N^+ -BSF layer, a PCE of greater than 13.6% was achieved with a c-Si thickness of only about $20 \mu\text{m}$. The excellent device performance was ascribed to the superior optical property, the improved heterojunction, the reduced back contact resistance, and the effective suppression of the recombination on both surfaces. This study opens a design guideline for high-performance hybrid solar cells with ultrathin absorbers, which can potentially reduce the cost of solar cells and provide added features of light weight and flexibility for the extended applications.

EXPERIMENTAL SECTION

Back-Side N^+ Layer Diffusion. The c-Si films were thinned from one-side-polished n-type (100) bulk Si wafers ($3-5 \Omega \cdot \text{cm}$, $270 \mu\text{m}$ thickness, Czochralski-grown), using KOH solution with a concentration of 50 wt % at 80°C . The thickness of a thinned c-Si film is shown in Supporting Information Figure S1. The back-side highly doped N^+ layer was produced through conventional diffusion using phosphoryl chloride (POCl_3) gas. The diffusion was conducted at 850°C for 45 min. The diffusion depth and sheet resistance were measured to be about $0.3 \mu\text{m}$ and $85 \Omega \text{ sq}^{-1}$, respectively. Before the diffusion process, thin film samples were cleaned using a standard RCA procedure. Initially, the thinned films were cleaned by immersing in a mixed solution of H_2SO_4 and H_2O_2 with a volume ratio of 3:1 at 100°C for 10 min. Subsequently, the samples were rinsed with deionized (DI) water and immersed in a solution of H_2O_2 (30%), HCl (37%), and DI water in a volume ratio of 1:1:6 at 80°C for 10 min, followed by a DI water bath. Finally, the samples were cleaned using a HF (2%) solution for 60 s to remove the native oxide. After the described cleaning procedure, the polished side of the

thin films was coated with 100 nm SiN_x as a protection layer for one-side diffusion. After the diffusion process, the samples were immersed in a HF (2%) solution for 2 min to remove the back-side phosphorus silicate glass (PSG) and the front-side O-rich SiN_x layer.

Nanostructure Fabrication. The procedure for conventionally structured SiNPs followed a previous report.²⁴ The hierarchically bowl-like Si nanostructures (nanopores) on the polished surface were fabricated using a novel MaCE process in a mixed solution of 7.5 mM AgNO_3 , 4 vol % of HF, and 0.36 vol % of H_2O_2 and DI water for 60 s at room temperature. The back side of the c-Si films was protected by nail enamel during etching. After the etching process, Si films were immersed in concentrated HNO_3 for 3 min to remove the silver nanoparticles deposited on Si films. The back cover was removed using acetone and ethanol. Then the structured thin films were etched in a second round using the same etchant, followed by a silver and nail enamel removal.

Hybrid Solar Cell Fabrication. After being cleaned by the standard RCA procedure as described above, the thin films (with or

without nanostructures) were spin-coated with the PEDOT:PSS (Clevios PH1000) solution mixed with dimethyl sulfoxide (5%) and Zonyl fluorosurfactant (0.1%) at a spin speed of 1000 rpm for 60 s to form a heterojunction. Then the samples were annealed on a hot plate at 140 °C for 20 min to remove the solvents and formed a highly conductive p-type organic thin film. Ag electrodes with a 150 nm thickness were deposited on both sides of the sample by thermal evaporation.

Sample Characterization. The morphological analysis of the samples was conducted by scanning electron microscopy (Hitachi S-4800) and transmission electron microscopy (Tecnai F20). Crystal structure was determined by imaging with a high-resolution TEM and SAD (Tecnai F20). The reflectance was measured by a UV/vis/NIR spectrometer (Lambda 950, PerkinElmer) in the wavelength range of 300–1100 nm. A detached silver mirror reflecting layer was placed under the samples while reflectance was measured. Thus, the transmission was neglected when measuring the reflectance. The PV performance was measured with a solar simulator (Oriel, Sol3A) under AM1.5 illumination (100 mW/cm²). The detailed test conditions are shown in the Supporting Information. The external quantum efficiency curves were measured by a quantum efficiency measurement system (Oriel, IQE-200TM). The capacitances versus voltage (*C–V*) measurements were carried out with a Keithley 4200-SCS semiconductor parameter analyzer. The minority carrier lifetime was measured by microwave photoconductivity decay (WT-2000 μ PCD, Semilab).

Conflict of Interest: The authors declare no competing financial interest.

Acknowledgment. This work is supported by National Natural Science Foundation of China (Grant No. 61404144), Zhejiang Provincial Natural Science Foundation (Grant No. LY14F040005), Natural Science Foundation of Ningbo (Grant No. 2013A610030) “Thousand Young Talents Program” of China, One Hundred Person Project of the Chinese Academy of Sciences, the Instrument Developing Project of the Chinese Academy of Sciences (Grant No. yz201328). The authors thank Prof. Xin Chen for reflectance spectrum characterization.

Supporting Information Available: Conditions of current–voltage curves test. Thickness measurement of *c-Si* film after the thinning process. Cross-sectional view of the conventionally structured SiNPs and the conventional-SiNPs covered with PEDOT:PSS film. Reflection spectra of 20 μ m thick *c-Si* films textured with conventional-SiNPs, one-round structured SiNPs, two-round reconstructed-SiNPs, and the flat one. Additional TEM images of the SiNP/PEDOT:PSS interface at the bottom and side wall position of SiNPs. Dark *J–V* characteristics of the thin film Si/PEDOT:PSS HJSCs with different surface texturing. Real device images while testing. The Supporting Information is available free of charge on the ACS Publications website at DOI: 10.1021/acsnano.5b02432.

REFERENCES AND NOTES

- Sailor, M. J.; Ginsburg, E. J.; Gorman, C. B.; Kumar, A.; Grubbs, R. H.; Lewis, N. S. Thin-Films of N-Si/Poly-(CH₃)₃Si-cyclooctatetraene: Conduction-Polymer Solar Cells and Layered Structures. *Science* **1990**, *249*, 1146–1149.
- Shen, X. J.; Sun, B. Q.; Liu, D.; Lee, S. T. Hybrid Heterojunction Solar Cell Based on Organic–Inorganic Silicon Nanowire Array Architecture. *J. Am. Chem. Soc.* **2011**, *133*, 19408–19415.
- Jeong, S.; Garnett, E. C.; Wang, S.; Yu, Z. G.; Fan, S. H.; Brongersma, M. L.; McGehee, M. D.; Cui, Y. Hybrid Silicon Nanocone-Polymer Solar Cells. *Nano Lett.* **2012**, *12*, 2971–2976.
- Zielke, D.; Pazidis, A.; Werner, F.; Schmidt, J. Organic-Silicon Heterojunction Solar Cells on n-Type Silicon Wafers: The BackPEDOT Concept. *Sol. Energy Mater. Sol. Cells* **2014**, *131*, 110–116.
- Nagamatsu, K. A.; Avasthi, S.; Jhaveri, J.; Sturm, J. C. A 12% Efficient Silicon/PEDOT:PSS Heterojunction Solar Cell Fabricated at < 100 °C. *IEEE J. Photovoltaics* **2014**, *4*, 260–264.
- Zhang, J.; Song, T.; Shen, X. L.; Yu, X. G.; Lee, S. T.; Sun, B. Q. A 12%-Efficient Upgraded Metallurgical Grade Silicon–Organic Heterojunction Solar Cell Achieved by a Self-Purifying Process. *ACS Nano* **2014**, *8*, 11369–11376.
- Kim, J.; Yoon, S. Y.; Choi, K. Effects of Phosphorus Diffusion Gettering on Minority Carrier Lifetimes of Single-Crystalline, Multi-crystalline and UMG Silicon Wafer. *Curr. Appl. Phys.* **2013**, *13*, 2103–2108.
- Jeong, S.; McGehee, M. D.; Cui, Y. All-Back-Contact Ultra-thin Silicon Nanocone Solar Cells with 13.7% Power Conversion Efficiency. *Nat. Commun.* **2013**, *4*, 2950–2956.
- Wang, S.; Weil, B. D.; Li, Y. B.; Wang, K. X. Z.; Garnett, E.; Fan, S. H.; Cui, Y. Large-Area Free-Standing Ultrathin Single-Crystal Silicon as Processable Materials. *Nano Lett.* **2013**, *13*, 4393–4398.
- Fossum, J. G.; Nasby, R. D.; Pao, S. C. Physics Underlying the Performance of Back-Surface-Field Solar Cells. *IEEE Trans. Electron Devices* **1980**, *27*, 785–791.
- Yu, P.; Tsai, C.-Y.; Chang, J.-K.; Lai, C.-C.; Chen, P.-H.; Lai, Y.-C.; Tsai, P.-T.; Li, M.-C.; Pan, H.-T.; Huang, Y.-Y.; et al. 13% Efficiency Hybrid Organic/Silicon-Nanowire Heterojunction Solar Cell via Interface Engineering. *ACS Nano* **2013**, *7*, 10780–10787.
- Liu, R.; Lee, S.-T.; Sun, B. 13.8% Efficiency Hybrid Si/Organic Heterojunction Solar Cells with MoO₃ Film as Antireflection and Inversion Induced Layer. *Adv. Mater.* **2014**, *26*, 6007–6012.
- Thomas, J. P.; Leung, K. T. Defect-Minimized PEDOT:PSS/Planar-Si Solar Cell with Very High Efficiency. *Adv. Funct. Mater.* **2014**, *24*, 4978–4985.
- Zhang, Y. F.; Cui, W.; Zhu, Y. W.; Zu, F. S.; Liao, L. S.; Lee, S. T.; Sun, B. Q. High Efficiency Hybrid PEDOT:PSS/Nanostructured Silicon Schottky Junction Solar Cells by Doping-Free Rear Contact. *Energy Environ. Sci.* **2015**, *8*, 297–302.
- Zhang, Y. F.; Zu, F. S.; Lee, S. T.; Liao, L. S.; Zhao, N.; Sun, B. Q. Heterojunction with Organic Thin Layers on Silicon for Record Efficiency Hybrid Solar Cells. *Adv. Energy Mater.* **2014**, *4*, 1300923.
- Schmidt, J.; Titova, V.; Zielke, D. Organic-Silicon Heterojunction Solar Cells: Open-Circuit Voltage Potential and Stability. *Appl. Phys. Lett.* **2013**, *103*, 183901.
- He, L. N.; Lai, D.; Wang, H.; Jiang, C. Y.; Rusli High-Efficiency Si/Polymer Hybrid Solar Cells Based on Synergistic Surface Texturing of Si Nanowires on Pyramids. *Small* **2012**, *8*, 1664–1668.
- Thiyagu, S.; Hsueh, C. C.; Liu, C. T.; Syu, H. J.; Lin, T. C.; Lin, C. F. Hybrid Organic–Inorganic Heterojunction Solar Cells with 12% Efficiency by Utilizing Flexible Film-Silicon with a Hierarchical Surface. *Nanoscale* **2014**, *6*, 3361–3366.
- Wei, W. R.; Tsai, M. L.; Ho, S. T.; Tai, S. H.; Ho, C. R.; Tsai, S. H.; Liu, C. W.; Chung, R. J.; He, J. H. Above-11%-Efficiency Organic–Inorganic Hybrid Solar Cells with Omnidirectional Harvesting Characteristics by Employing Hierarchical Photon-Trapping Structures. *Nano Lett.* **2013**, *13*, 3658–3663.
- Jeong, H.; Song, H.; Pak, Y.; Kwon, I. K.; Jo, K.; Lee, H.; Jung, G. Y. Enhanced Light Absorption of Silicon Nanotube Arrays for Organic/Inorganic Hybrid Solar Cells. *Adv. Mater.* **2014**, *26*, 3445–3450.
- Fossum, J. G.; Burgess, E. L. High-Efficiency P⁺-N-N⁺ Back-Surface-Field Silicon Solar Cells. *Appl. Phys. Lett.* **1978**, *33*, 238–240.
- Singh, S. N.; Jain, G. C. Effect of the Back-Surface Field on the Open-Circuit Voltages of P⁺-N-N⁺ and N⁺-P-P⁺ Silicon Solar Cells. *Sol. Cells* **1982**, *5*, 143–172.
- Huang, Z. P.; Geyer, N.; Werner, P.; de Boor, J.; Gosele, U. Metal-Assisted Chemical Etching of Silicon: A Review. *Adv. Mater.* **2011**, *23*, 285–308.
- Oh, J.; Yuan, H.-C.; Branz, H. M. An 18.2%-Efficient Black-Silicon Solar Cell Achieved through Control of Carrier Recombination in Nanostructures. *Nat. Nanotechnol.* **2012**, *7*, 743–748.
- Bai, F.; Li, M. C.; Song, D. D.; Yu, H.; Jiang, B.; Li, Y. F. Metal-Assisted Homogeneous Etching of Single Crystal Silicon: A Novel Approach To Obtain an Ultra-thin Silicon Wafer. *Appl. Surf. Sci.* **2013**, *273*, 107–110.

26. Geyer, N.; Fuhrmann, B.; Leipner, H. S.; Werner, P. Ag-Mediated Charge Transport during Metal-Assisted Chemical Etching of Silicon Nanowires. *ACS Appl. Mater. Interfaces* **2013**, *5*, 4302–4308.
27. Gao, P.; Wang, H.; Sun, Z.; Han, W.; Li, J.; Ye, J. Efficient Light Trapping in Low Aspect-Ratio Honeycomb Nanobowl Surface Texturing for Crystalline Silicon Solar Cell Applications. *Appl. Phys. Lett.* **2013**, *103*, 253105.
28. Zhu, Y. W.; Song, T.; Zhang, F. T.; Lee, S. T.; Sun, B. Q. Efficient Organic–Inorganic Hybrid Schottky Solar Cell: The Role of Built-in Potential. *Appl. Phys. Lett.* **2013**, *102*, 113504.